

A Complete Brain Model (fix)

¹Alexandra Warner, ¹Chris Johnson

¹University of Utah, Salt Lake City UT; ²Placeholder in case we need to put more refs

July 18, 2017

Abstract

Here is some abstract text

1 Introduction

Cardiac ischemia occurs when an imbalance develops within the myocardium in which the demand for oxygen and nutrients exceeds local supply.¹ Under ischemic conditions, cardiac tissue undergoes structural, metabolic, ionic, and neurochemical changes, which lead to, among other consequences, electrical changes within the heart that can be monitored via electrocardiogram (ECG) measurements. Consequently, ECG markers, in particular shifts in the ST segment, have been used clinically to identify patients with myocardial ischemia; however, variability in the presentation of ischemia, (*i.e.* location, size, and geometry) hinders the ECG, diagnostic accuracy of ischemic heart disease, leading to errors in clinical assessment.

It is generally accepted that ST segment elevations are associated with fully transmural ischemia and myocardial infarction (MI), whereas ST segment depressions are regarded as markers of subendocardial ischemia.² Diagnostics based on ST segment shifts, however, yield relatively poor sensitivity and specificity when assessing myocardial ischemia. As a result, testing strategies in both acute care settings and office visits often result in erroneous disease identification. For instance, studies have found that hospitals tend to over-admit patients with suspected MI or ischemic disease. In one study, as many as 72% of cardiac ICU admissions for MI did not suffer from the condition.³ Aside from acute diagnosis and triage environments, such as hospitals and emergency departments, patients may undergo exercise stress testing to determine if a supply/demand imbalance exists under conditions of elevated stress. These tests have similarly low sensitivity (68%) and specificity (77%) in terms of ECG-based prediction.⁴ Poor sensitivity and specificity markers suggest that current understanding regarding ischemia, and the electrical consequences associated with it, is incomplete.

To address this gap in understanding, computational forward simulation approaches have been developed to study the progression of ischemia and its resulting electrical outcomes. The general formulation of such models involves the imposition of a bioelectric source, or sources, within a passive volume conductor. Electric fields generated by the applied sources extend to the cardiac or body surface, which represents the solution space. Such models have been useful in elucidating some

of the causes of electrical ST segment shifts created by ischemia, but uncertainty associated with the condition still exists, particularly with regard to nontransmural cases. This uncertainty is due, in part, to simplifications employed in the various modeling techniques, particularly with regard to source representations. The selection of an appropriate source model is essential to produce useful forward simulations, and many representations have emerged, including single dipole models, current wavefront patterns, transmembrane potential differences, etc. For purposes of this study, we limit our ischemia model sources to multidimensional, geometric zones that are represented by transmembrane potential differences embedded within the cardiac geometry.

Due to the structure of the myocardium, and specifically the susceptibility of the endocardium to ischemic conditions,^{5–7} it is broadly accepted that the ischemic region initiates along the endocardial surface and expands transmurally until reaching the epicardial wall.⁸ As a result, almost all simulations of nontransmural (or partial thickness) ischemia have maintained the endocardially centered source paradigm, with only few exceptions.^{9,10} In most cases, only the shape of the ischemic region varies. For instance, several groups have chosen to use quadrilateral (2D) or hexahedral (3D) source representations of the ischemic zone, largely due to simplicity in imposing such shapes within their chosen cardiac model.^{11–14} Other groups have used circular or spherical regions,^{15–17} and still others have applied a more endocardial-conforming ellipsoidal shape.^{18,19}

Though parameterized shapes, such as spheres and cubes, are preferred for complex computational modeling, they do not fully reflect the spatial complexity of the ischemic region as it develops. Experimental observations show that ischemia does not develop as a simplistic shape, centered along the endocardium. Rather, an ischemic region often originates as multiple, smaller regions that expand over time to form larger, more transmural ischemic zones.^{20–22} Furthermore, it has been observed that ischemic development is more often dispersed throughout the myocardial tissue rather than centered along the endocardium during the first several minutes of ischemia.²²

In this study, we present a forward model that incorporates more realistic ischemic zone geometry and compare those results with those produced by common ischemic zone representations. Experimental recordings of induced ischemia were used to validate the proposed method before comparisons were made between these results and those produced by reconstructions of the three most used ischemic zone representations (spheres, hexahedra, and conforming ellipsoids). We show that the common source representations of ischemic development inadequately represent the true complexity of the condition. *{To be completed}*

2 Methods

2.1 Data Acquisition

2.2 Registration

2.3 Segmentation

2.4 Diffusion Weighted Images

2.5 Functional MRI

2.6 Meshing

2.7 Simulations

2.8 Mathematical Modeling

2.9 Numerical Methods

2.9.1 Experimental Methods

We induced episodes of acute, transient ischemia in anesthetized, open-chest swine ($n = ??$) and canine ($n = ??$) preparations. In each experiment, the heart was exposed and suspended in a pericardial cradle. A portion of the LAD was minimally dissected and fitted with a hydraulic occluder, which could be compressed to restrict coronary blood flow, thereby creating the transient ischemic condition, and then released to restore normal cardiac perfusion. Experimental protocols consisted of measuring extracellular potentials, both on the epicardial surface and within the myocardium, while applying stepwise increases of ischemic load.²³ To this end, two basic protocols were used to induce ischemia: 1) LAD blood flow was incrementally reduced by the occluder while maintaining a constant, often elevated, heart rate (supply ischemia) or 2) increases in the heart rate were applied while maintaining a constant, often restricted, LAD blood flow (demand ischemia). For purposes of this study, we do not consider the differences between supply and demand ischemia but rather focus on the size, shape, and location of the zones within the heart that show an electrical response to the ischemic condition. All studies were performed in accordance with the Guide for the Care and Use of Laboratory Animals (NIH Pub. No 85-23, Revised 1996).

Customized sock and needle electrodes were used to acquire electrical recordings of both epicardial and intramural electrical potentials. A 247-electrode, flexible sock array,²⁴ with recording electrodes evenly distributed across the ventricles, acquired epicardial electrogram recordings. Twenty-five (25) flexible fiberglass plunge needles²⁵ were used to record intramural electrical activity. Plunge needles were constructed with 10 evenly spaced electrodes at 1.6 mm intervals along the shaft. Needles were placed in and around the perfusion bed of the occluded LAD. Sock and needle recordings were made periodically at a 1KHz sampling rate, the combination of which provided a *3-dimensional* electrical representation of the induced ischemic condition.

In addition to the acquisition of electrical recordings, digitized locations of sock electrodes and needle locations were extracted for postexperiment validation studies. After digitization, needle

electrodes were removed and replaced with radio-opaque spacers prior to cardiac imaging in order to provide a registration reference.

Electrograms were calibrated, gain adjusted, and baseline corrected against control recordings, which had been taken immediately before each intervention. Poor quality electrograms, caused by broken lead connections or bad contacts, as well as electrograms without positive Q-wave deflections (identified as cavity electrodes) were discarded. The global root mean squared signal was computed from data recordings of both sock and needle electrodes. These signals were used to identify a point that lay at 40% of the distance between the J point and T wave peak (ST40%). Potential difference maps were generated at ST40%, which compared baseline recordings to those obtained during an ischemic episode. Potential differences, taken at ST40% during baseline conditions, were used to generate a threshold by which ischemic regions were identified as values exceeding two standard deviations. Sock recordings were used to validate simulation findings and will be addressed later. Needle electrodes were used to generate subject-specific ischemic zone geometries by identifying regions within a spatial neighborhood that met the above-mentioned ischemic thresholding criteria.²⁶

2.10 Simulation Pipeline

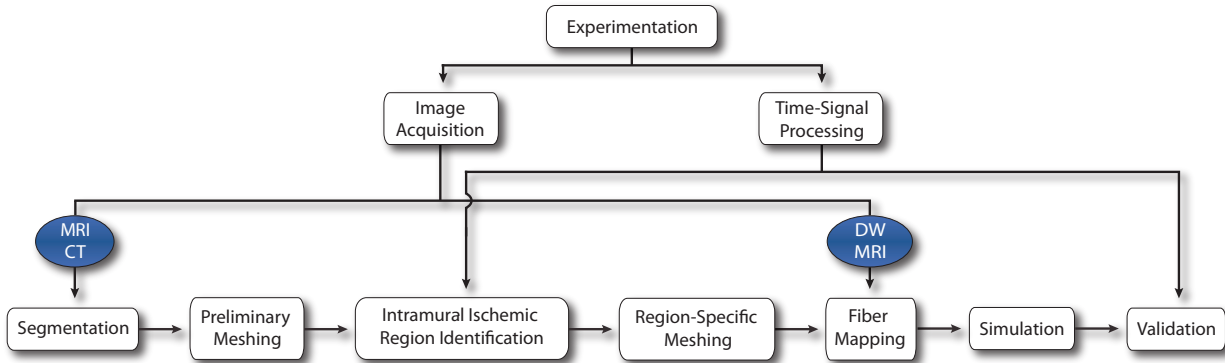


Figure 1: Ischemia Simulation Pipeline. Both image and time signals were extracted from experimental protocols of acute, induced ischemic preparations. Image data was used to generate geometries through segmentation and meshing. Intramural electrical data, recorded from plunge needles, were mapped to these meshes to define ischemic zone location. New meshes were generated with ischemic geometries imposed on which ischemic simulations were generated and validated against the original experimental data recorded from epicardial sock data.

A simulation pipeline was implemented in order to produce in silico models that were representative of experimental findings. Electrical data acquired during the experimental process, as well as imaging information acquired post experiment, were used to construct subject-specific, finite element, bioelectric simulations by way of the steps illustrated in Figure 1.

2.10.1 Imaging and Segmentation

After completion of the experimental protocol, each heart was excised and scanned with a 7 tesla MRI scanner using FISP and FLASH MRI sequences. Diffusion tensor images (DTI) were also ac-

quired to determine fiber direction. FISP scans rendered consistent, albeit low, contrast throughout the tissue - preserving edges near the field of view boundaries. FLASH scans, in comparison, provided images of high contrast within the center of the volume, which diminished steeply near the field of view boundaries. The advantages of both FISP and FLASH were combined in order to produce realistic, geometric segmentations of blood, cardiac tissue, and needles, using the Seg3D* open-source software package. Needle locations were readily identified within the scans as dark regions occupied by the radio-opaque spacers that were inserted at the end of the experimental phase. Diffusion-weighted MRI (DW-MRI) images were also obtained from which fiber orientation was derived.

2.10.2 Geometric Processing and Data Mapping

Segmentations were used to generate realistic *3-dimensional* geometries for use in subsequent finite element simulations (See Section 2.2.4). By using two open-source meshing packages, we were able to generate smooth, linear, subject-specific, boundary-conforming, tetrahedral meshes for use in simulations. First, segmentations were ported into the BioMesh3D* software package to generate smoothed/tightened surface representations. BioMesh3D surface representations were used as input indicator functions to a second meshing package, Cleaver*, from which the final mesh was derived. Cleaver is a multimaterial meshing package that produces structured meshes of tetrahedral elements with guaranteed minimum element angles,²⁷ resulting in quality meshes that require fewer computational resources. Cleaver, however, does not offer the surface-tightening features of BioMesh3D. As a result, meshes produced by Cleaver from standard MRI segmentations (with no surface tightening) would propagate the stair-stepped surfaces inherent in rasterized, volumetric data. By combining packages, we were able to produce smooth, structured meshes of guaranteed element quality.

Correspondence points derived from known sock and needle locations were used to register needle and sock electrode geometries within the cardiac mesh using the SCIRun problem-solving environment †. Processed data values were mapped to corresponding node locations within the cardiac mesh. Linear interpolation to local nodes was applied but restricted to the geometric convex hull of the needle locations. Extrapolation to outlying regions, not within the scope of needle locations, was not included.

To identify ischemic zones, potential difference maps were generated that removed baseline potentials from those observed during ischemic interventions. Difference map values within the specified needle region that exceeded a value greater than two standard deviations from baseline recordings were identified and labeled as ischemic. These new label masks were used to create a final mesh that contained three defined tissues (blood, healthy cardiac tissue, and ischemic cardiac tissue) that shared conforming surfaces - an important feature in static forward simulations when considering areas in proximity to potential sources.²⁸

Finally, subject-specific fiber orientation was applied within the mesh. A vector field was defined by the principle eigenvector from DW-MRI images with all other cross-sectional fiber components regarded as isotropic. This vector field was normalized, aligned, and mapped to the cardiac mesh using weighted-average interpolation to provide a basis for anisotropic conductivity.

*<http://sci.utah.edu/software.html>

Table 1: Ratio applied to tensor conductivity values within healthy and ischemic regions.²⁹

Conductivity Labels	Healthy Conductivity Values	Ischemic Conductivity Values
σ_{el}	1	1/2
σ_{il}	1	1
σ_{et}	1/3	1/4
σ_{it}	1/20	1/20
σ_b	3	3

2.10.3 Mathematical Modeling

The cardiac mesh, with associated fiber structure and ischemic region, was used to solve the bidomain passive current flow equation:

$$\nabla \cdot (\bar{\sigma}_e + \bar{\sigma}_i) \nabla \phi_e = -\nabla \cdot \bar{\sigma}_i \nabla V_m \quad (1)$$

where σ_e and σ_i represent the extracellular and intracellular conductivity tensors, respectively. ϕ_e is the extracellular potentials, and V_m represents the transmembrane potential.

In this model, it was assumed that the heart was surrounded by a perfect insulator, leading to a Neumann boundary condition on the epicardial surface. The endocardium, in contrast, allowed for extracellular, but not intracellular, current flow into the ventricular blood pool. Initial blood potentials were defined by Cauchy boundary conditions along the endocardial surface as shown in Equation 2.

$$\begin{cases} \nabla \cdot (\bar{\sigma}_e + \bar{\sigma}_i) \nabla \phi_e = -\nabla \cdot \bar{\sigma}_i V_m & x \in \Omega_H \\ \vec{n}_{epi} \cdot (\bar{\sigma}_e + \bar{\sigma}_i) \nabla \phi_e = 0 & x \in \partial\Omega_{H,epi} \\ \vec{n}_{endo} \cdot (\bar{\sigma}_e \nabla \phi_e) = -\vec{n}_b \cdot (\bar{\sigma}_b \nabla \phi_b) & x \in \partial\Omega_{H,endo} \\ \phi_e = \phi_b & x \in \partial\Omega_{H,endo} \\ \phi_i = 0 & x \in \Omega_b \end{cases} \quad (2)$$

where Ω_H represents the cardiac volume; $\partial\Omega_{H,epi}$ and $\partial\Omega_{H,endo}$ the epicardial and endocardial surfaces, respectively; ϕ_e and ϕ_b correspond to potentials in the extracellular space and the blood, respectively. \vec{n} represents the normal, outward unit vector along the epicardial (*epi*), endocardial (*endo*), and blood (*b*) surfaces. The first equation specifies the relationship between transmembrane and extracellular potentials within the cardiac domain. The following four equations define the handling of currents and potentials along the cardiac surfaces. The blood, in all studies, was completely enclosed within the cardiac region and considered to have isotropic conductivity (See Figure 2 and Table 1).

Conductivity values within the tissue, as well as the blood pool, were normalized with respect to extracellular longitudinal values and matched those used in previous studies.^{10,29,30} Table 1 shows the conductivity values used for this study. These conductivity values were chosen to be consistent with those previously defined by Johnston and Kilpatrick.³¹ Conductivities within the ischemic region were reduced with respect to healthy values corresponding to the first 5 - 15 minutes after ischemic onset.

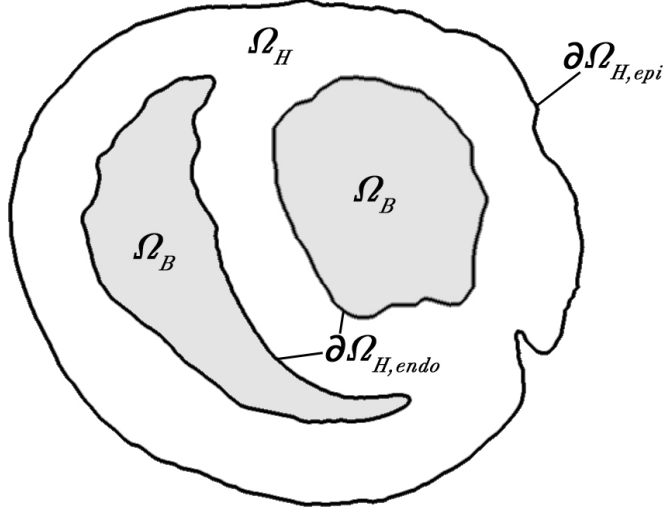


Figure 2: Bidomain equations are defined within the cardiac tissue Ω_H and bounded by epicardial and endocardial boundaries $\Omega_{H,epi}$ and $\Omega_{H,endo}$. Extracellular currents were allowed to flow into the blood volume Ω_B along the endocardial boundary.

We defined a fixed transmembrane potential value (V_m) of 30mV as the potential source for our forward simulations. The reduced transmembrane potential mimics the delayed activation of diseased tissue under ischemic conditions during the ST-segment. Healthy tissue was assigned a value of 0 mV, typical of the relatively quiescent state of healthy cardiac activation during the ST segment. Between healthy and ischemic tissue, a border zone was defined in which potentials progressed from the diseased to healthy states.

The border zone, the region between healthy and ischemic tissue, has been determined to be a necessary, and problematic, region to include in simulation studies.^{10, 29, 32} In this study, we defined the border zone as a piecewise, continuous function represented by Equation 3 in which a Gaussian function defines the region from the ischemic zone boundary to a specified transition point, S_1 . At S_1 the border transitions to a linear, decreasing function that reduces to 0 (the value assigned to healthy tissue) at S_2 . It is important to note that not all models, found in the literature, have applied border zones. For the sake of consistency and uniformity, however, we have imposed border regions into all of the forward simulations constructed in this paper. Table 2 shows the values applied to Equation 3 for this study.

$$BZ = \begin{cases} V_m e^{\frac{-d^2}{2\sigma^2}} & d < S_1 \\ \Gamma - \frac{\Gamma}{S_2 - S_1}(d - S_1) & S_1 \leq d < S_2 \\ 0 & d \geq S_2 \end{cases} \quad (3)$$

$$\text{where } \Gamma = V_m e^{\frac{-(S_1)^2}{2\sigma^2}}$$

Table 2: Values Used In Border Zone Determination.

Label	Definition	Value
V_m	Transmembrane Potential	30 mV
σ	Gaussian RMS Width	5 mm
S_1	First Transition Distance	8 mm
S_2	Second Transition Distance	11 mm
d	<i>distance</i>	<i>variable</i>

2.10.4 Numerical Methods

Solutions to Equation 1 were computed using finite element methods. By applying Green's divergence theorem to Equation 1, the following weak formulation is generated

$$\int ((\bar{\sigma}_e + \bar{\sigma}_i) \nabla \phi_e) \cdot \nabla \psi(\bar{x}) d\bar{x} = - \int (\bar{\sigma}_i \nabla V_m) \cdot \nabla \psi(\bar{x}) d\bar{x}, \quad \forall \psi \in \Omega \quad (4)$$

where, Ω (see Section Section 2.2.2) is the linear, finite element mesh, ψ represents the finite element basis functions characterized by local hat functions associated with mesh nodes. By applying this formulation to the finite dimensional mesh, we can reduce Equation 4 to a system of linear equations

$$A\phi_e = -RV_m \quad (5)$$

where A and R represent stiffness matrices defined by $A_{j,k} = \langle \nabla \psi_j, (\bar{\sigma}_e + \bar{\sigma}_i) \nabla \psi_k \rangle_\Omega$ and $R_{j,k} = \langle \nabla \psi_j, \bar{\sigma}_i \nabla V_m \rangle_\Omega$, while ϕ_e and V_m represent extracellular and transmembrane potentials, respectively.³³

We used the open-source, SCIRun problem solving environment³⁴ to apply parameters and to solve Equation 5 numerically. Within the SCIRun environment, fiber orientation and conductivity tensors were applied to the mesh, initial and boundary conditions were defined, and border regions were generated in order to compute extracellular potentials by way of a conjugate gradient method with a Jacobi preconditioner.

2.10.5 Comparison Approaches

Epicardial potentials compared using CC, RMS Error, and DICE correlation...Do it first, then explain it.

2.10.6 Validation

In order to validate solutions of the ischemic condition, experimental data was compared to simulated solutions. Experimental data were mapped to the mesh by digitizing and later registering sock electrodes to points identified on the surface of the cardiac mesh. Potential data from sock electrodes were interpolated onto the ventricular surfaces and compared to simulated potentials on a node-to-node correspondence. RMS error and the correlation coefficient between simulated epicardial potentials and experimental sock data were generated to assess accuracy of simulation results.

3 Results

4 Discussion

Write Me

5 Conclusion

Write Me

6 Acknowledgements

Support for this research comes from the the NIH NCRR Center for Integrative Biomedical Computing (www.sci.utah.edu/cibc), NIH NCRR Grant No. 5P41-RR012553-08, the Nora Eccles Treadwell Foundation, and the Richard A. and Nora Eccles Harrison Fund for Cardiovascular Research.

References

- [1] D. Hearse. Myocardial ischaemia: Can we agree on a definition for the 21st century? *Cardiovascular Research*, 28:1737–1744, 1994.
- [2] R P Holland and H Brooks. Precordial and epicardial surface potentials during myocardial ischemia in the pig. A theoretical and experimental analysis of the TQ and ST segments. *Circulation Research*, 37(4):471–480, 1975.
- [3] T H Lee, G W Rouan, M C Weisberg, D A Brand, E F Cook, D Acampora, and L Goldman. Sensitivity of routine clinical criteria for diagnosing myocardial infarction within 24 hours of hospitalization. *Ann. Intern. Med.*, 106(2):181–186, 1987.
- [4] R. Gianrossi, R. Detrano, D. Mulvihill, K. Lehmann, P. Dubach, A. Colombo, D. McArthur, and V. Froelicher. Exercise-induced ST depression in the diagnosis of coronary artery disease. A meta-analysis. *Circulation*, 80:87–98, 1989.
- [5] P.F. Salisbury, C.E. Cross, and P.A. Rieben. Acute ischemia of inner layers of the ventricular wall. *American Heart Journal*, 66:650–656, 1963.
- [6] T.W. Moir. Subendocardial distribution of coronary blood flow and the effect of antianginal drugs. *Circulation Research*, 30:621–627, 1972.
- [7] J.K. Kjekshus, P.R. Maroko, and B.E. Sobel. Distribution of myocardial injury and its relation to epicardial ST segment changes after coronary artery occlusion in the dog. *Cardiovascular Research*, 6:490–499, 1972.
- [8] K.A. Reimer, J.E. Lowe, M.M. Rasmussen, and R.B. Jennings. The wavefront phenomenon of ischemic cell death. Myocardial infarct size vs duration of coronary occlusion in dogs. *Circulation*, 56:786–794, 1977.
- [9] Bjrn Fredrik Nielsen, Xing Cai, Joakim Sundnes, and Aslak Tveito. Towards a computational method for imaging the extracellular potassium concentration during regional ischemia. *Mathematical Biosciences*, 220(2):118–130, 2009.
- [10] D J Swenson, J G Stinstra, B M Burton, K K Aras, L J Healy, and R S MacLeod. Evaluating the effects of border zone approximations with subject specific ischemia models. *World Congress on Medical Physics and Biomedical Engineering, September 7 - 12, 2009, Munich, Germany*, 25/4(Chapter 446):1680–1683, 2010.
- [11] Bruce Hopenfeld, Jeroen G Stinstra, and Rob S Macleod. The effect of conductivity on ST-segment epicardial potentials arising from subendocardial ischemia. *Ann Biomed Eng*, 33(6):751–763, 2005.
- [12] P R Johnston, D Kilpatrick, and C Y Li. The importance of anisotropy in modeling ST segment shift in subendocardial ischaemia. *IEEE Trans. Biomed. Eng.*, 48(12):1366–1376, 2001.
- [13] P Colli Franzone, L F Pavarino, and Simone Scacchi. Dynamical effects of myocardial ischemia in anisotropic cardiac models in three dimensions. *Mathematical Models and* , 17(12):1965–2008, 2007.

- [14] X Jie, V Gurev, and N Trayanova. Mechanisms of mechanically induced spontaneous arrhythmias in acute regional ischemia. *Circulation Research*, 106(1):185–92, 2010.
- [15] Mary C MacLachlan, Joakim Sundnes, Ola Skavhaug, Marius Lysaker, Bjrn Fredrik Nielsen, and Aslak Tveito. A linear system of partial differential equations modeling the resting potential of a heart with regional ischemia. *Mathematical Biosciences*, 210(1):238–252, 2007.
- [16] B Trénor, L Romero, JM Ferrero, J Sáiz, G Moltó, and JM Alonso. Vulnerability to reentry in a regionally ischemic tissue: a simulation study. *Ann Biomed Eng*, 35(10):1756–70, 2007.
- [17] M Wilhelms, O Dssel, and G Seemann. Simulating the impact of the transmural extent of acute ischemia on the electrocardiogram. *Computers In Cardiology. Proceedings*, pages 13–16, 2010.
- [18] D D Li, C Y CY Li, A C AC Yong, and D D Kilpatrick. Source of electrocardiographic ST changes in subendocardial ischemia. *Circulation Research*, 82(9):957–970, 1998.
- [19] Andrew J Pullan, Martin L Buist, Greg B Sands, Leo K Cheng, and Nicolas P Smith. Cardiac electrical activity-from heart to body surface and back again. *Journal of Electrocardiology*, 36:63–67, 2003.
- [20] R.B. Jennings, C.E. Ganote, and K.A. Reimer. Ischemic tissue injury. *American Journal of Pathology*, 81:179–198, 1975.
- [21] C. Steenbergen, C. Deleeuw, C. Barlow, B. Chance, and J.R. Williamson. Heterogeneity of the hypoxic state in perfused rat heart. *Circulation Research*, 41:606–615, 1977.
- [22] K.K. Aras. *Bioelectric Source Characterization Of Acute Myocardial Ischemia*. PhD thesis, The University of Utah, 2015.
- [23] K. Aras, B. Burton, D. Swenson, and R. MacLeod. Sensitivity of epicardial electrical markers to acute ischemia detection. *J Electrocardiol*, 47(6):836–841, 2014.
- [24] G. Arisi, E. Macchi, C. Corradi, R.L. Lux, and B. Taccardi. Epicardial excitation during ventricular pacing: Relative independence of breakthrough sites from excitation sequence in canine right ventricle. *Circ Res*, 71(4):840–849, 1992.
- [25] J.M. Rogers, S.B. Melnick, and J. Huang. Fiberglass needle electrodes for transmural cardiac mapping. *IEEE Trans Biomed Eng*, 49(12):1639–1641, 2002.
- [26] K.K. Aras, S. Shome, D.J. Swenson, J.G. Stinstra, and R.S. MacLeod. Electrocardiographic response of the heart to myocardial ischemia. In *Computers in Cardiology 2009*, pages 105–108, 2009.
- [27] J. Bronson, J.A. Levine, and R.T. Whitaker. Lattice cleaving: a multimaterial tetrahedral meshing algorithm with guarantees. *IEEE Transactions on Visualization and Computer Graphics (TVCG)*, pages 223–237, 2014.
- [28] D. Swenson, J.A. Levine, Z. Fu, J.D. Tate, and R.S. MacLeod. The effect of non-conformal finite element boundaries on electrical monodomain and bidomain simulations. *Computing in Cardiology*, (37):97–100, 2010.

- [29] B. Hopenfeld, J.G. Stinstra, and R.S. MacLeod. Mechanism for ST depression associated with contiguous subendocardial ischemia. *J Cardiovasc Electrophysiol*, 15(10):1200–1206, 2004.
- [30] J.G. Stinstra, B. Hopenfeld, and R.S. MacLeod. A model for the passive cardiac conductivity. *Int. J. Bioelectromag.*, 5(1):185–186, 2003.
- [31] P R Johnston. A cylindrical model for studying subendocardial ischaemia in the left ventricle. *Mathematical Biosciences*, 2003.
- [32] D Kilpatrick, P R Johnston, and D S Li. Mechanisms of ST change in partial thickness ischemia. *Journal of Electrocardiology*, 2003.
- [33] Dafang Wang, Robert M Kirby, Rob S Macleod, and Chris R Johnson. Inverse electrocardiographic source localization of ischemia: An optimization framework and finite element solution. *Journal of Computational Physics*, 250:403–424, 2013.
- [34] S G Parker and C R Johnson. SCIRun: A scientific programming environment for computational steering, 1995.